Electronic Supplementary Material (ESI) for Energy & Environmental Science.
This journal is © The Royal Society of Chemistry 2023

Supporting Information for

"Embedded, micro-interdigitated flow fields in high areal-loading intercalation electrodes towards seawater desalination and beyond"

Vu Q. Do,[a] Erik R. Reale,[a] Irwin Loud IV,[a] Paul G. Rozzi,[a] Haosen Tan,[b] David A. Willis,[b] and Kyle C. Smith[a,c,d,e,*]

a. Department of Mechanical Science and Engineering, University of Illinois at Urbana-Champaign, Urbana, IL, USA

b. Department of Mechanical Engineering, Southern Methodist University, Dallas, TX, 75275

c. Department of Materials Science and Engineering, University of Illinois at Urbana-Champaign, Urbana, IL, USA

d. Computational Science and Engineering Program, University of Illinois at Urbana-Champaign, Urbana, IL, USA

e. Beckman Institute for Advanced Science and Technology, University of Illinois at Urbana-Champaign, Urbana, IL, USA

*corresponding author: kcsmith@illinois.edu

Table of Contents

Modeled Comparison of Desalination using Different Flow Fields

Using the flowing porous electrode theory implemented in Refs. 1,2 and using the same model parameters described therein, we conducted simulations to compare the salt removal dynamics of representative flow-by configurations (both flow behind and flow between) to a flow-through configuration as shown in Fig. S1. As we demonstrate using other modeling in the main text and later in the SI, appropriately designed interdigitated flow fields produce flow *through* electrodes, rather than flow *by* electrodes. In contrast, the serpentine and parallel flow-field designs that have been used in fuel cells and flow batteries previously do not primarily produce flow through porous electrodes. Hence, the purpose of the present porous electrode theory modeling is to illustrate the impact of flow-through versus flow-by electrodes on the electrochemical transport processes that occur when used in a symmetric FDI device for desalination.

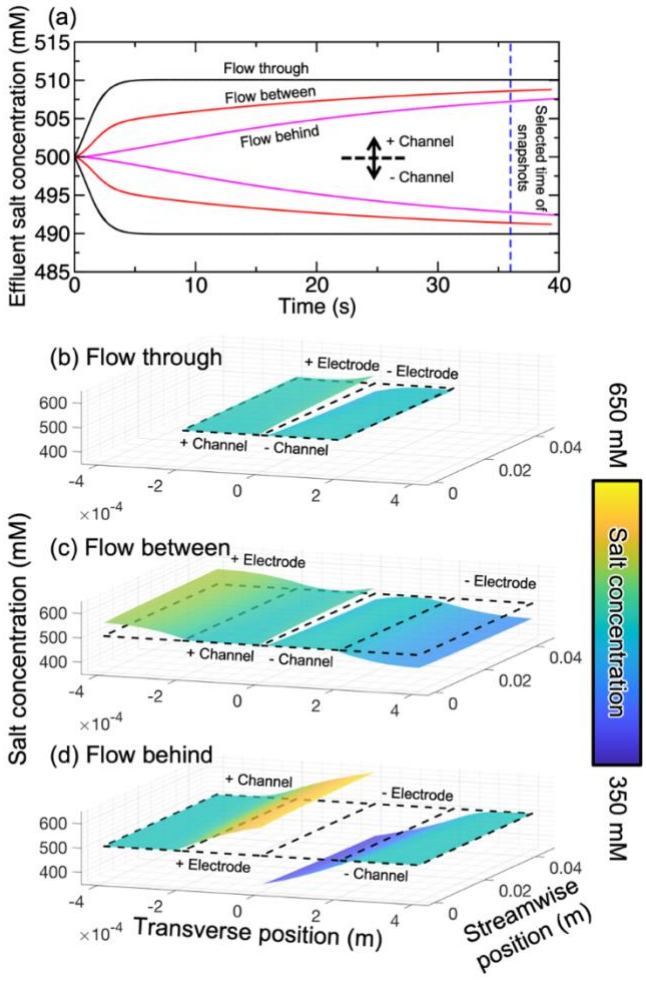

Figure S1: Simulated response at 4 mA cm^{-2} applied current density for electrodes having 16 mg cm^{-2} loading and 45 mm x 45 mm electrode area for flow-through and flow-by configurations. (a) Effluent salt concentration versus time. Spatial distribution of salt concentration for (b) flow-through, (c) flow-between, and (d) flow-behind configurations.

To this end Fig. S1b,c shows that in flow-by configurations salt is removed from solution that is stagnant, rather than from flowing solution. As a result, larger concentration differences persist in the transverse direction across flow-by electrodes (Figs. S1b,c) in comparison with flow-through electrodes (Fig. S1d). The impact of these effects is reduced desalination efficiency, because of the more lagged response of the effluent concentration produced by flow-by configurations relative to flow-through configurations (Fig. S1a). Hence, flow-by configurations, such as those engendered by serpentine and parallel flow fields, are likely to experience substantial losses to salt removal due to this effect. In contrast, the solution within electrodes is efficiently evacuated from the electrodes when a flow-through configuration is used (see Figure S1b).

Asymptotic Scaling of Apparent Permeability

The flow rate through a channel due to a pressure difference between the inlet and outlet plane $\Delta p = p_{in} - p_{out}$ (Fig. S2a) can be expressed using Darcy's law if the hydraulic resistance within channels is neglected (in all other modeling that follows after this section – both numerical and analytical – we relax this simplifying assumption):

$$Q = Q_1 + Q_2 = 2Q_1 = 2\frac{k_h^{pe}}{\mu}\frac{\Delta p}{s} A_{in} = 2\frac{k_h^{pe}}{\mu}\frac{\Delta p}{s} hL_{ch} \qquad (*)$$

Considering the same section of the electrode, Darcy's law also relates the flow rate through this section with its apparent permeability k_h^{app} and the pressure drop Δp, as illustrated in Fig. S2b:

$$Q = \frac{k_h^{app}}{\mu}\frac{\Delta p}{L_e} A_{in} = \frac{k_h^{app}}{\mu}\frac{\Delta p}{L_e}[2(s+w)h] \qquad (**)$$

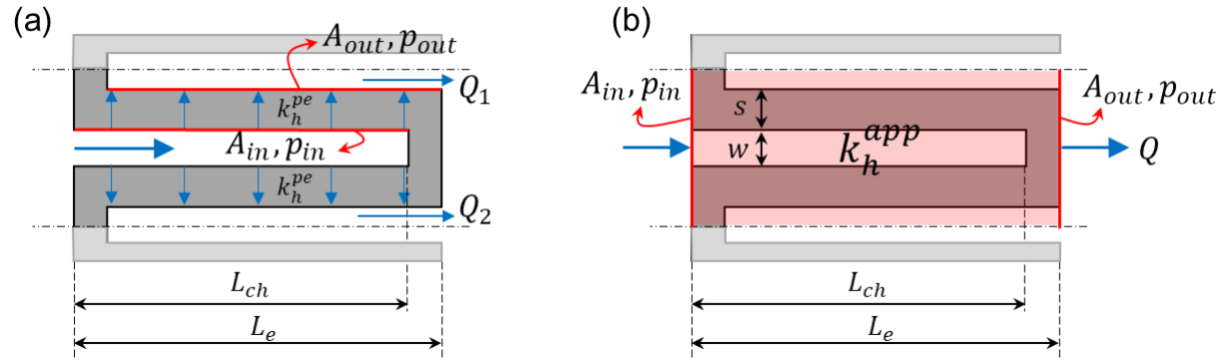

Figure S2: (a) Flow rate through a channel when considering the porous electrode hydraulic permeability k_h^{pe}. (b) Flow rate through a section of a patterned electrode when considering its apparent permeability k_h^{app}. Here, w is channel width, s is inter-channel spacing, h is electrode thickness, L_{ch} is channel length, and L_e is electrode length. A is area, p is pressure, and in and out subscripts denote inlets and outlets.

Equating (1) and (2) we obtain the following scaling for the normalized apparent permeability in this limit of vanishing hydraulic resistance within channels:

$$k_{h,max}^{app,*} = \frac{k_{h,max}^{app}}{k_h^{pe}} = \frac{L_e L_{ch}}{s(s+w)}$$

Here, we denote this quantity as $k_{h,max}^{app,*}$ because an upper bound to apparent permeability is produced when the hydraulic resistance within channels is neglected. The above relation shows that if we keep constant electrode length L_e and channel length L_{ch}, and if we also fix the coverage fraction of the electrode material for the IDFF (i.e, $s/w =$ constant), then the improvement in apparent hydraulic permeability due to IDFF embedding scales with the inverse square of channel width:

$$k_{h,max}^{app,*} = \frac{k_{h,max}^{app}}{k_h^{pe}} = \frac{L_e L_{ch}}{w^2 \alpha(\alpha+1)}$$

Numerical Model for Flow-Through Electrodes Embedded with eμ-IDFFs

When designing an eμ-IDFF, there are three dimensions that we varied: channel width w, inter-channel distance s, and channel length L_{ch}. The last of these dimensions determines the gap g between the end of the channel and the edge of the electrode. The objective of choosing the dimension of a given eμ-IDFF is to ensure even distribution of flow through the electrode microstructure while minimizing material loss. To model these effects, we implemented a finite-volume solver in MATLAB to simulate a Darcy-Darcy model for the 2D superficial velocity $\vec{u}_s$ inside porous electrodes that uses a permeabilty k_h^{pe} within porous electrode regions and that uses a permeability k_h^{ch} in channel regions. k_h^{ch} was determined from the Boussinesq solution for Poiseuille flow in rectangular cross-section channel with h-by-l size[4]:

$$Q = \frac{k_h^{ch} A}{\mu} \nabla p = \frac{hl\nabla p}{\mu}\left[\frac{h^2}{12} - \frac{16h^3}{l\pi^5}\sum_{n=1}^{\infty}\frac{1}{(2n-1)^5}\frac{\cosh(\beta_n l)-1}{\sinh(\beta_n l)}\right]$$

where Q is flow rate, p is pressure, and A is area normal to flow in the channel. This results in the following expression for k_h^{ch}:

$$k_h^{ch} = \frac{h^2}{12} - \frac{16h^3}{l\pi^5}\sum_{n=1}^{\infty}\frac{1}{(2n-1)^5}\frac{\cosh(\beta_n l)-1}{\sinh(\beta_n l)} \qquad (S5)$$

We solve the discrete equations obtained using the Finite Volume Method (FVM) using an iterative linear solver based on the Aggregation Based Algebraic Multigrid (AGMG) method.[5–7]

When electrode permeability and porosity are kept constant, a large gap g produces regions between channel tips and electrode edges where streamlines are

absent, indicating that fluid does not flow through electrode material and instead bypasses those regions (Fig. S3). Hence, small g is desirable to eliminate such dead zones. In addition, when g is fixed at 0.75 mm, increasing microchannel width and decreasing channel spacing leads to more uniform flow distribution through the porous electrode regions (Fig. S4).

The differences between the predicted apparent permeability and the measured apparent permeability for the electrodes used in our experiments (Fig. 2g in the main text) arise due to a number of reasons. Firstly, we assume that the permeability within porous electrode regions is uniform, when in fact the fabricated electrodes possess a certain level of heterogeneity in their permeability. For example, we observed electrodes to possess initial thickness before calendaring that can vary as much as 50 μm between the thinnest and the thickest regions, that is converted to a relative error in mass loading of $\sigma_{rel}(\Gamma) = 13\%$. In addition, when calculating porosity, we assumed that graphite foil thickness is maintained at 100 μm after calendaring. If it were compressed by 50% during calendering, the relative error of measured electrode thickness is $\sigma_{rel}(w_e) = 28\%$. The porosity, ε, depends on the electrode's density, ρ_e. Hence, the relative error of these quantities is the same: $\sigma_{rel}(\varepsilon) = \sigma_{rel}(\rho_e) = \sqrt{\sigma_{rel}^2(\Gamma) + \sigma_{rel}^2(w_e)} \approx 31\%$. These estimates of error are larger than the deviation between our predictions and experimental measurements, explaining the origin of these discrepancies at least in part. In addition, the model treats eμ-IDFFs as an infinite periodic array of channels, such that finite size effects are neglected, despite their presence in experimental patterns.

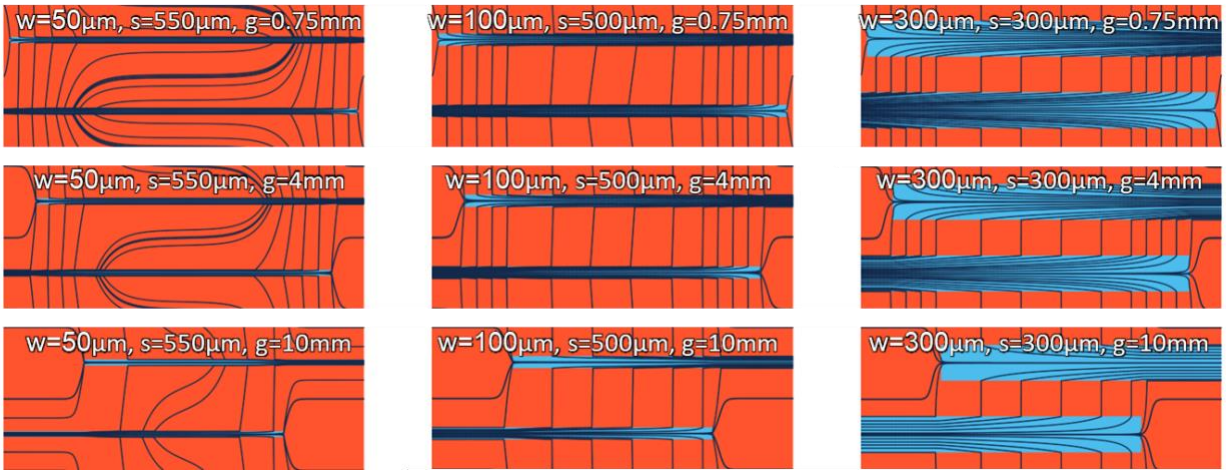

Figure S3. Streamlines of different interdigitated flow fields (eμ-IDFFs) with inter-channel distance s, channel width w, and gap between channel end and electrode edge g as shown. The electrode permeability and porosity in all cases are 0.28 μm^2 and 45%. Vertical and horizontal scaling are set differently to ease streamline visualization.

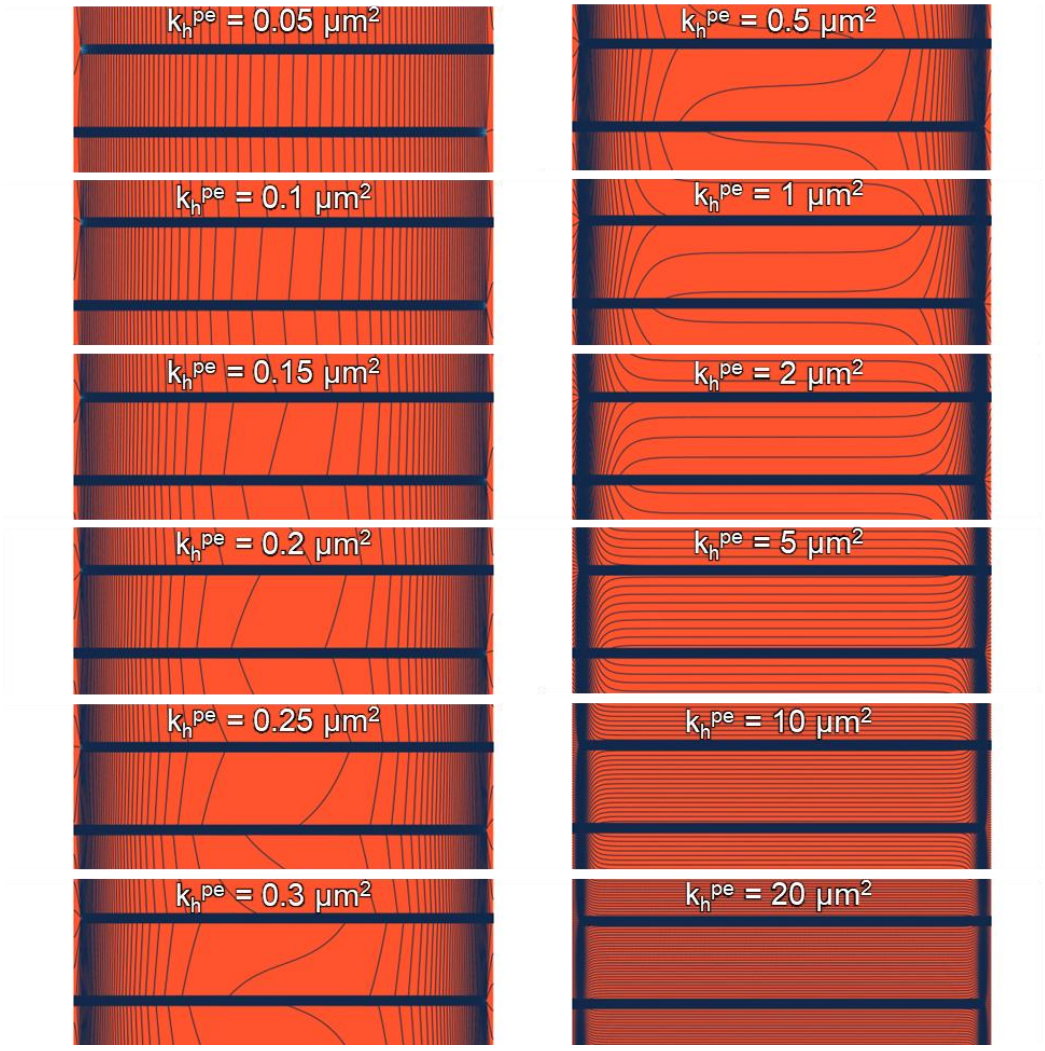

Figure S4: Streamlines of different interdigitated flow fields (eμ-IDFFs) with the same inter-channel distance (s = 530 μm), channel width (w = 70 μm), and gap between channel end and electrode edge (g = 750 μm). The electrode porosity in all cases was 45% but the porous electrode permeability k_h^{pe} was varied as shown.

Quasi-1D Analytical Model of IDFF Velocity and Permeability

Transverse Velocity Distribution

We now derive the transverse velocity distribution produced within a porous electrode containing an embedded, interdigitated flow field. In contrast with our numerical modeling described in the main text, the present simplified model that neglects velocity along channels within porous electrode material enables us to identify a key non-dimensional parameter that governs the transition among IDFF designs between a transverse flow-through velocity field to a parallel velocity field.

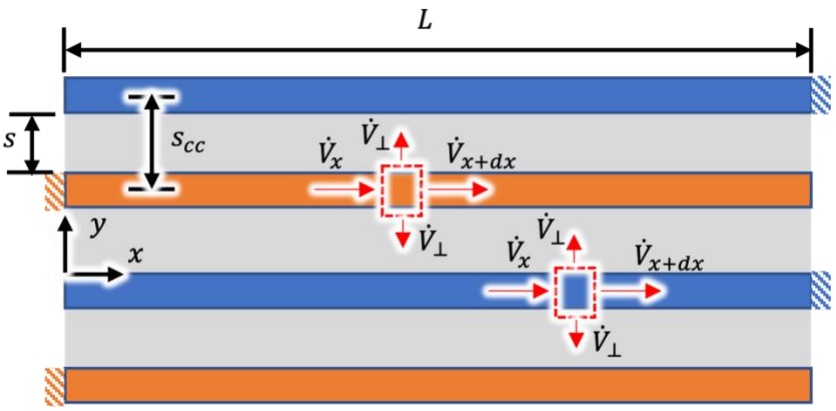

Figure S5: Schematic of an idealized interdigitated network of channels embedded within a porous electrode.

To derive this result, we apply conservation of fluid volume to a control volume of differential length dx on both high-pressure (blue) and low-pressure (orange) channels (Fig. S5) to arrive at the following:

$$\dot{V}_x - \dot{V}_{x+dx} - 2\dot{V}_\perp = 0$$

Using Taylor series expansion of volumetric flow along a given channel, we express an ordinary differential equation that couples the cross-section averaged superficial velocity along a given channel $\langle u_{s,\parallel} \rangle$ with the thickness-averaged superficial velocity transverse to the same channel $\langle u_{s,\perp} \rangle$:

$$A_c \frac{d\langle u_{s,\parallel} \rangle}{dx} + 2\langle u_{s,\perp} \rangle h = 0$$

Here, the cross-sectional area is A_c and thickness is h. We employ a Darcy-Darcy formulation (as already described) to relate these respective velocities to the associated pressure field. The superficial velocity along each channel depends on the channel's permeability k_h^{ch} and fluid viscosity μ:

$$\langle u_{s,\parallel} \rangle = -\frac{k_h^{ch}}{\mu} \frac{dp}{dx}$$

We model the transverse superficial velocity by neglecting x-direction contributions, in which case Darcy's law predicts linear variation of pressure with the y position coordinate:

$$\left|\langle u_{s,\perp}\rangle\right| = \frac{k_h^{pe}}{\mu}\frac{(p_H - p_L)}{s}$$

Here, k_h^{pe} is the hydraulic permeability of unpatterned porous electrode material and s is inter-channel distance that defines the span of porous electrode material between channels. Substitution of $\langle u_{s,\parallel}\rangle$ and $\langle u_{s,\perp}\rangle$ into the above volume conservation equation produces two ordinary differential equations (ODEs) that jointly govern pressure in high- and low-pressure channels.

$$\frac{k_h^{ch}A_c}{\mu}\frac{d^2p_H}{dx^2} - \frac{2k_h^{pe}h}{\mu s}(p_H - p_L) = 0$$

$$\frac{k_h^{ch}A_c}{\mu}\frac{d^2p_L}{dx^2} - \frac{2k_h^{pe}h}{\mu s}(p_L - p_H) = 0$$

We obtain a single ODE governing the position-dependent pressure difference between adjacent channels, $\theta = p_H - p_L$, by subtracting the above equations from each other:

$$\frac{d^2\theta}{dx^2} - \frac{4k_h^{pe}h}{k_h^{ch}sA_c}\theta = 0$$

The general solution to this equation is $\theta = c_1e^{-mx} + c_2e^{-mx}$ with $m = \left(4k_h^{pe}h/k_h^{ch}sA_c\right)^{0.5}$. While in experimental practice pressure is imposed on the left end of the high-pressure channel and on the right end of the low-pressure channel, the nature of the present governing equation demands a boundary condition for the difference in pressure between these channels. We therefore invoke a symmetry boundary condition for the pressure difference, such that $\theta(x = 0) = \theta(x = L) = \theta_0$. From this condition we obtain the variation of this pressure difference with position:

$$\theta(x) = \frac{\theta_0\left(\sinh\left(m(L - x)\right) + \sinh(mx)\right)}{\sinh(mL)}$$

This solution is then used directly to obtain the transverse superficial velocity distribution:

$$\langle u_{s,\perp}\rangle = \frac{k_h^{pe}\theta(x)}{\mu s} = \frac{\theta_0 k_h^{pe}}{\mu s}\frac{\left(\sinh\left(m(L - x)\right) + \sinh(mx)\right)}{\sinh(mL)}$$

This solution lends itself naturally to dimensionless form:

$$\frac{\langle u_{s,\perp}\rangle \mu s}{\theta_0 k_h^{pe}} = u_\perp^* = \frac{\left(\sinh\left(m^*(1-x/L)\right) + \sinh(m^* x/L)\right)}{\sinh(m^*)}$$

where $m^* = mL = \left(4k_h^{pe} hL^2 / k_h^{ch} sA_c\right)^{0.5}$.

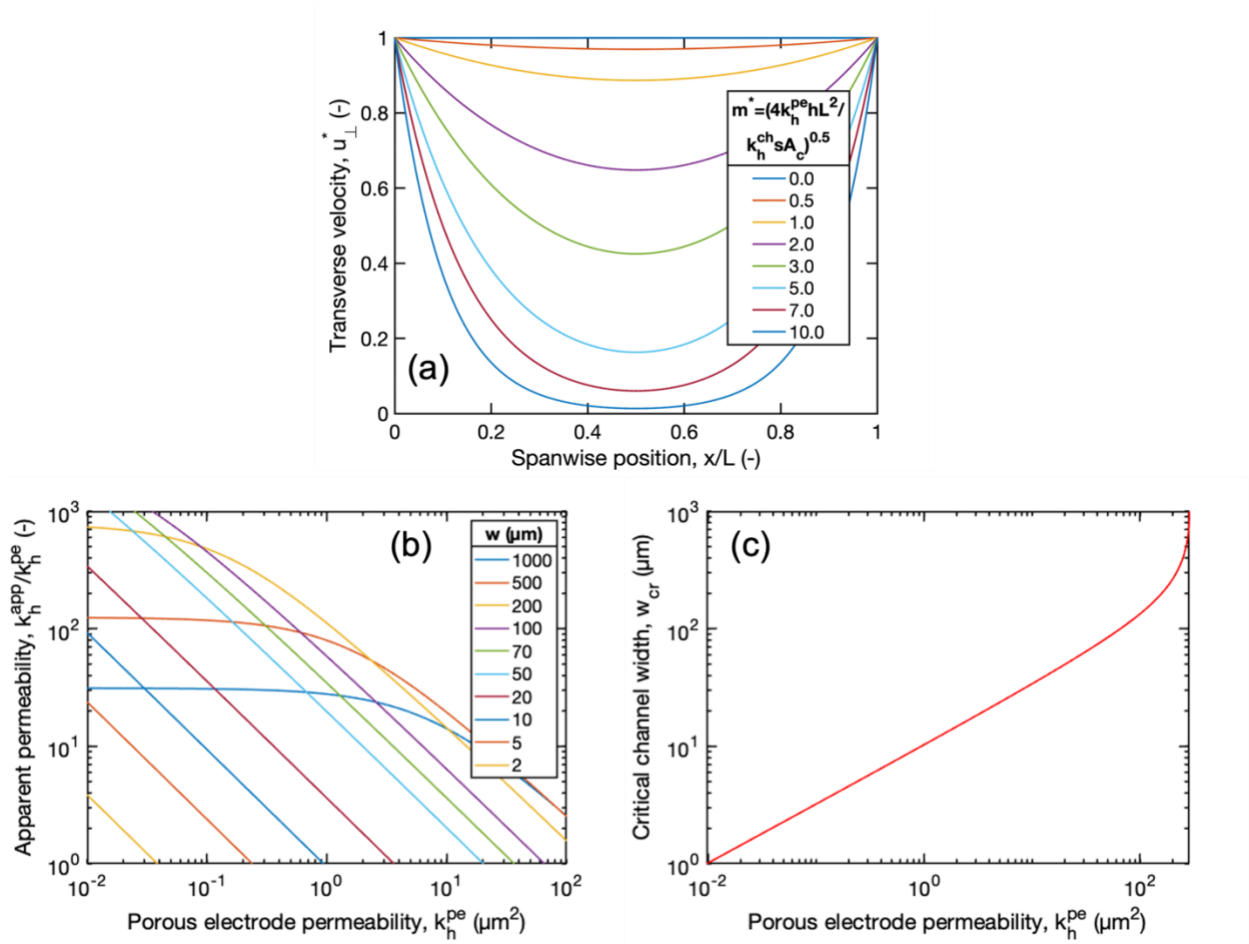

Figure S6: Predictions of the quasi-1D, analytical IDFF model. (a) Non-dimensional transverse velocity as a function of non-dimensional spanwise position for different m^* values. (b) Normalized apparent permeability versus porous-electrode permeability with 200 μm electrode thickness, 4.5 cm electrode length, and a width to inter-channel distance ratio of 13.2%=70μm/530μm. (c) Critical channel width as a function of porous electrode permeability using the dimensional constraints.

Examination of transverse velocity profiles in Fig. S6 reveals that $m^* \ll 1$ produces uniform flow through the porous electrode, whereas $m^* \geq 10$ produces a dead zone in the porous electrode at the center of its span. To derive a condition for the rational design

of such channels, we require $m^* \leq 7$, which assures that transverse velocity in the center of the porous electrode region is at least 5% of its value at the electrode's ends. For simplicity, we consider a channel cross-section that extends through the electrode's entire thickness h and for which the channel's width w is substantially smaller than the electrode's thickness ($w << h$), in which case $A_c = wh$ and $k_h^{ch} = w^2/12$. These assumptions produce $m^* = mL = \left(48 k_h^{pe} L^2/w^3 s\right)^{0.5}$. Alternatively, we define a dimensionless parameter $\Xi = k_h^{pe} L^2/(w^3 s)$,* which is the ratio of the characteristic longitudinal hydraulic resistance within channels to the characteristic transverse hydraulic resistance through porous electrode material. m^* depends on Ξ in the following way: $m^* = (48\Xi)^{0.5}$. Thus, the IDFF design criterion ($m^* \leq 7$) dictates the following condition for Ξ to assure flow-through functionality of the IDFF of interest:

$$\Xi = k_h^{pe} L^2/(w^3 s) \leq 49/48 \approx 1$$

As a result, we observe that this condition is more easily satisfied either by the electrode having low permeability, by increasing channel width, or by increasing inter-channel distance to reduce the magnitude of Ξ. In turn, one could also decrease channel length by decreasing electrode size to reduce Ξ, but doing so is expected to be impractical in many contexts.

Apparent Permeability

To derive an expression for the apparent permeability of the resulting IDFF we integrate the obtained transverse velocity to yield the total rate entering the high-pressure channel $\dot{V}_{ch}$:

$$\dot{V}_{ch} = 2h \int_0^L \langle u_{s,\perp} \rangle dx = \frac{2hk_h^{pe}\theta_0}{\mu s \sinh(mL)} \int_0^L \sinh\big(m(L-x)\big) + \sinh(mx) dx$$
$$= \frac{2hk_h^{pe}\theta_0}{\mu s m \sinh(mL)} \left[\cosh(mx) - \cosh\big(m(L-x)\big)\right]_0^L = \frac{4hk_h^{pe}\theta_0(\cosh(mL)-1)}{\mu s m \sinh(mL)}$$

This equation can be used to express θ_0 in terms of $\dot{V}_{ch}$:

$$\theta_0 = \mu s m \sinh(mL)\, \dot{V}_{ch} / \left[4hk_h^{pe}(\cosh(mL)-1)\right]$$

We then substitute the solution for $\theta(x)$ into the volume conservation equation for the high-pressure channel to obtain an integral equation for its pressure gradient:

* We use the symbol Ξ to denote this parameter because of its intuitive appeal resulting from its three parallel lines representing a high- and low-pressure channel separated by intervening porous electrode material.

$$\frac{dp_H}{dx} = \frac{2k_h^{pe} h\theta_0}{sk_h^{ch} A_c \sinh(mL)} \int \Big(\sinh\big(m(L-x)\big) + \sinh(mx)\Big)\, dx$$
$$\frac{dp_H}{dx} = \frac{2k_h^{pe} h\theta_0}{sk_h^{ch} A_c m \sinh(mL)} \big(\cosh(mx) - \cosh\big(m(L-x)\big) + \kappa\big)$$

Employing the no-flux boundary condition at the tip of the high-pressure channel subject to the Darcy's law ($dp_H/dx|_{x=L} = 0$), we find the constant of integration as $\kappa = 1 - \cosh(mL)$. Definite integration of the above pressure gradient yields the difference in pressure between the inlet and the tip of the high-pressure channel:

$$p_H(x=0) - p_H(x=L) = \frac{2k_h^{pe} h\theta_0 \big(mL(\cosh(mL)-1)\big)}{sk_h^{ch} A_c m^2 \sinh(mL)}$$

The total pressure difference $\Delta p = p_H(x=0) - p_H(x=L) + \theta_0$ reduces to the following after substituting θ_0 in terms of $\dot{V}_{ch}$:

$$\Delta p = \left(\frac{2k_h^{pe} h\big(mL(\cosh(mL)-1)\big)}{sk_h^{ch} A_c m^2 \sinh(mL)} + 1\right) \mu s m \sinh(mL)\, \dot{V}_{ch} / \big[4hk_h^{pe}(\cosh(mL)-1)\big]$$

The apparent permeability of the interdigitated network is thereby expressed as:

$$k_h^{app} \equiv \frac{\dot{V}_{ch}\mu}{2hs_{cc}} \frac{L}{\Delta p} = \frac{4hk_h^{pe} L(\cosh(mL)-1)}{2\left(\frac{2k_h^{pe} h\big(mL(\cosh(mL)-1)\big)}{sk_h^{ch} A_c m^2 \sinh(mL)} + 1\right) mhs_{cc} s \sinh(mL)}$$

Here, $s_{cc} = s + w$ is the center-to-center span between channels. Further simplification using the definition of m yields the following expression for the normalized apparent permeability k_h^{app}/k_h^{pe}, as predicted by this quasi-1D model:

$$\frac{k_h^{app}}{k_h^{pe}} = k_{h,max}^{app,*} \frac{4(\cosh(m^*)-1)}{(m^*)^2(\cosh(m^*)-1) + 2(m^*)\sinh(m^*)}$$
$$= k_{h,max}^{app,*} \frac{4(\coth(m^*) - \operatorname{csch}(m^*))}{(m^*)^2(\coth(m^*) - \operatorname{csch}(m^*)) + 2m^*}$$

Here, $k_{h,max}^{app,*} = L^2/[s(s+w)]$ is the upper bound of normalized apparent permeability derived in the limit of vanishing hydraulic resistance within channels when $L = L_{ch} \approx L_e$, as described in our asymptotic scaling analysis that precedes this section.

Laser-Patterning of Intercalation Electrodes

Engraving Procedures

As stated in the main text, a channel width of 70 μm, a spacing between two channels of 530 μm, and a channel depth of 200 μm was chosen for our eμ-IDFFs. Hence,

over the electrode area of 4.5×4.5 cm consists of 74 microchannels, as shown in Fig. S7. To engrave this eμ-IDFF into our electrodes, a Trotec Speedy 400 Flexx laser was used. This instrument is a dual head laser engraver with a CO_2 laser and a 50W Yb- doped fiber laser, but only the fiber laser head was used.

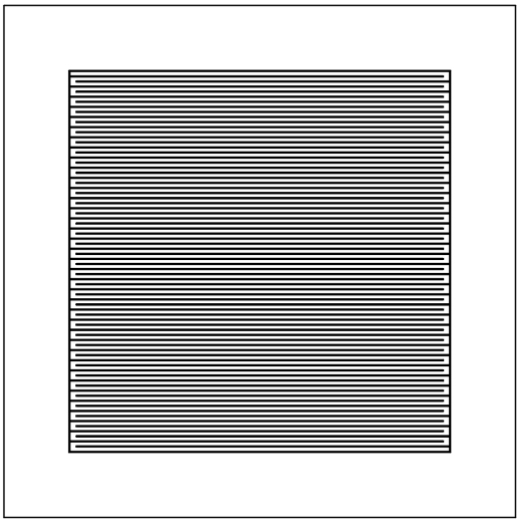

Figure S7: A sketch of the full eμ-IDFF that was engraved into electrodes. The dimension across the eμ-IDFF is 4.5 cm.

Channels were engraved by moving the laser along a series of parallel passes. For all laser passes, 20% of the maximum laser power (50W) was used with the speed of the laser being 1 m s^{-1} and the repetition rate being 100 kHz. These settings result in a fluence of 0.895 J cm^{-2} (± 0.158 J cm^{-2}), which was calculated as $P\tau/A_{spot}$, where P is the laser power, A_{spot} is the area of the laser spot, and τ is the laser pulse width. A_{spot} was estimated using averaged diameter of holes that were ablated in an 8 μm thick sheet of aluminum foil (All-Foils, Inc.) (Fig. S8). These discrete holes were obtained by increasing the laser power and the scanning speed to space out the laser pulse train. The average hole diameter was determined to be 11.9 $\pm$ 1.2 μm. Since the specific pulse width of the Trotec laser could not be easily found, we assumed the pulse width to be 100 ns, which falls within the range reported in the manual (1-1000 ns).

Figure S8: Laser ablation of holes in 8 µm thick aluminum with measured hole diameters.

To create a single channel with sufficient width and depth, three adjacent laser passes were performed on the electrode of interest with a spacing of 25 µm between the path that defined each pass, as depicted in Fig. S9. These three adjacent laser paths were repeated twice to create a given channel.

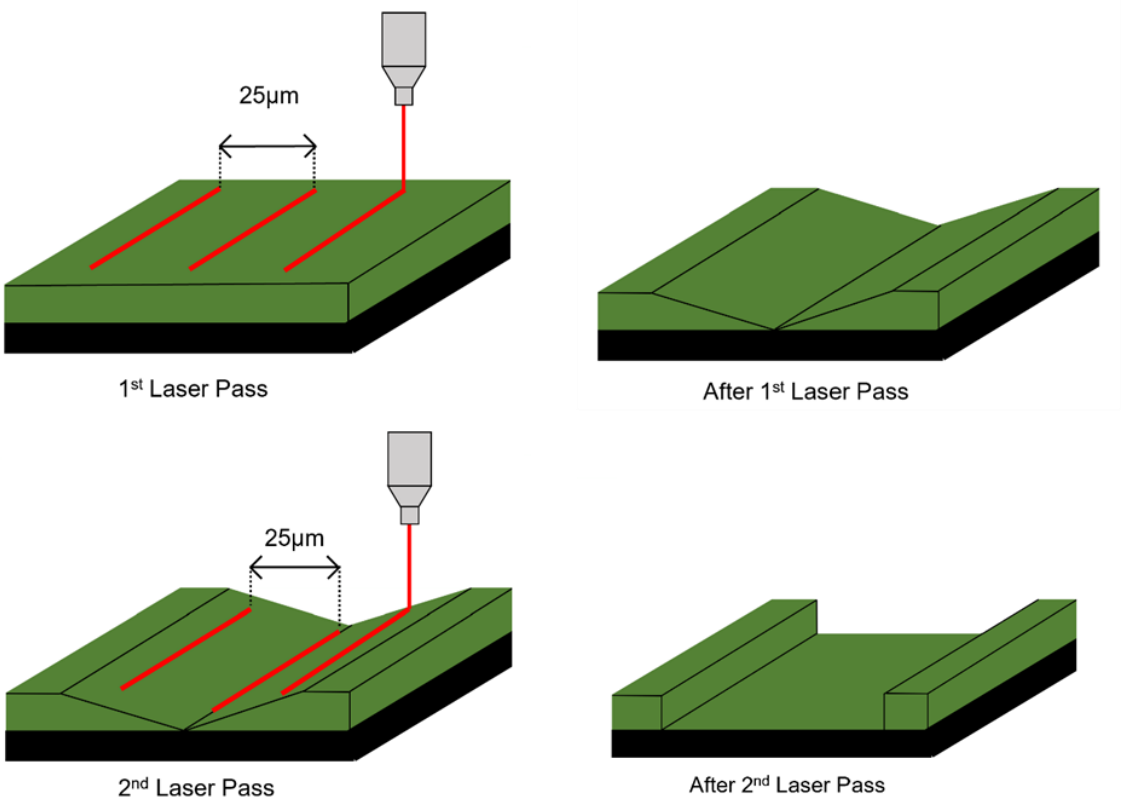

Figure S9: Idealized schematic for the engraving of a single microchannel. With the above mentioned fluence, the laser ablates the electrode composite (green) but does not cut through the graphite (black).

Engraving of Water-Imbibed Electrodes for Improved Channel Quality

Prior to engraving, the pores of all samples were imbibed with deionized (DI) water to improve channel resolution and smoothness. As shown in Fig. S10, the channels produced on water-imbibed electrodes were consistently smaller than those produced on dry electrodes at the same laser power, regardless of whether they were made with three laser passes or one. In addition, the root-mean-square roughness along the centerline and side walls of the channels were lower when the water imbibed approach was used (Fig. S11).

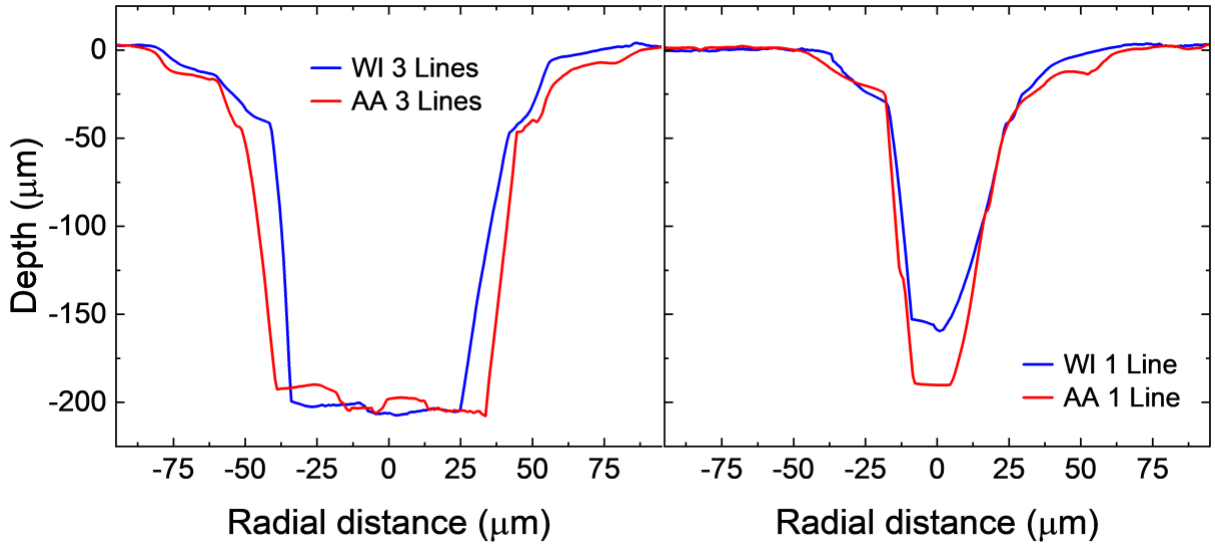

Figure S10: Example of cross-sections of channels produced on water-imbibed (WI) electrodes and dry electrodes with air assisted (AA) using three laser paths (left) and one laser path (right).

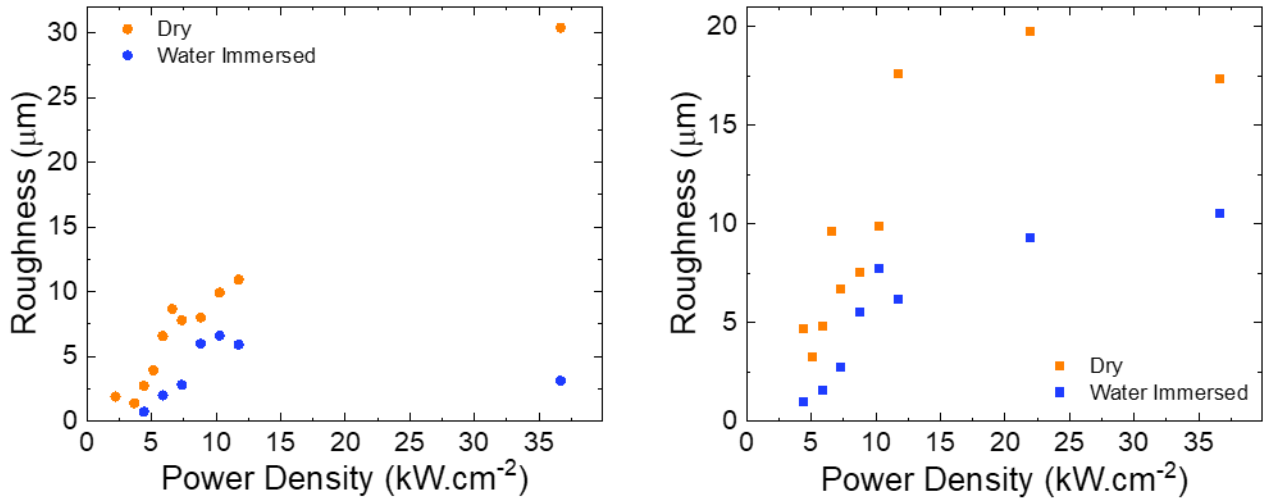

Figure S11: Root-mean-square roughness along the centerline (left) and sidewalls (right) of channels created with water-imbibed and dry electrodes at various laser power densities.

eμ-IDFF Characterization

The geometry and microstructure of channels were characterized using a laser profilometer (Keyence VK-X1000 3D Laser Scanning Confocal Microscope). As mentioned in the main text, three pairs of electrodes with different PBA loading levels (15 mg cm^{-2}, 19 mg cm^{-2}, and 21 mg cm^{-2}) were fabricated and patterned with the chosen eμ-IDFF design. Profilometry was performed on one electrode of each pair to characterize the resulting eμ-IDFF. The ideal channel shape was a rectangular channel with a width and depth of 70 μm and 200 μm, respectively, but the actual channel shape was trapezoidal (Fig. S10) due to the laser beam having a certain divergence angle and a certain intensity distribution. Hence, the cross-sectional area of the channel was a more effective classification parameter, since similar cross-sectional area would lead to similar pressure drop according to Darcy's law.

Three images were taken of each electrode, including two images of the channels near the corners of each electrode and one image of a channel at the center of each electrode. Even with consistent laser processing settings, we observed variability of these dimensions across a given electrode. The channels in the corners of the electrodes had consistently higher cross-sectional areas than the center. Table S5 shows the cross-sectional areas for the electrodes.

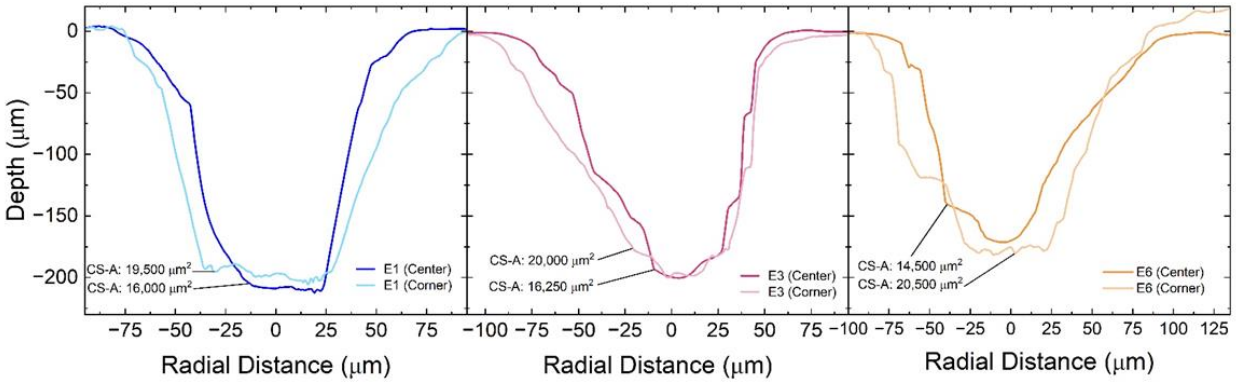

Figure S12: Channel profiles near the edge and in the center of electrodes with PBA loading of 15 mg cm^{-2} (left), 19 mg cm^{-2} (middle), and 21 mg cm^{-2} (right). The cross-section area (CS-A) for each profile are shown in the plot.

Fig. S12 shows how the channels at the corners of the electrodes have a systematically larger cross-sectional area than at the center. The x and y directions of the Trotec Speedy 400 Flexx laser are controlled by a mechanical gantry system. At the beginning and end of the cutting paths the gantry system will have some amount of mechanical inertia. Since the laser fires during the entire laser path, the laser will spend more time at the end of the channels as it accelerates and decelerates due to this inertia. This effect likely resulted in a larger cross-sectional area at the edges and corners of the electrodes.

Table S1: Statistics of cross-sectional areas of channels of three engraved electrodes

Electrode sample	Cross-section area (corner) (μm^2)			Cross-section area (center) (μm^2)		
	Max	Min	Med	Max	Min	Med
L1	21000	18000	19500	17000	15000	16000
M3	22000	18000	20000	17000	15500	16250
H6	22000	19000	20500	15500	13500	14500

Design and Layout of the FDI Flow Cell Used

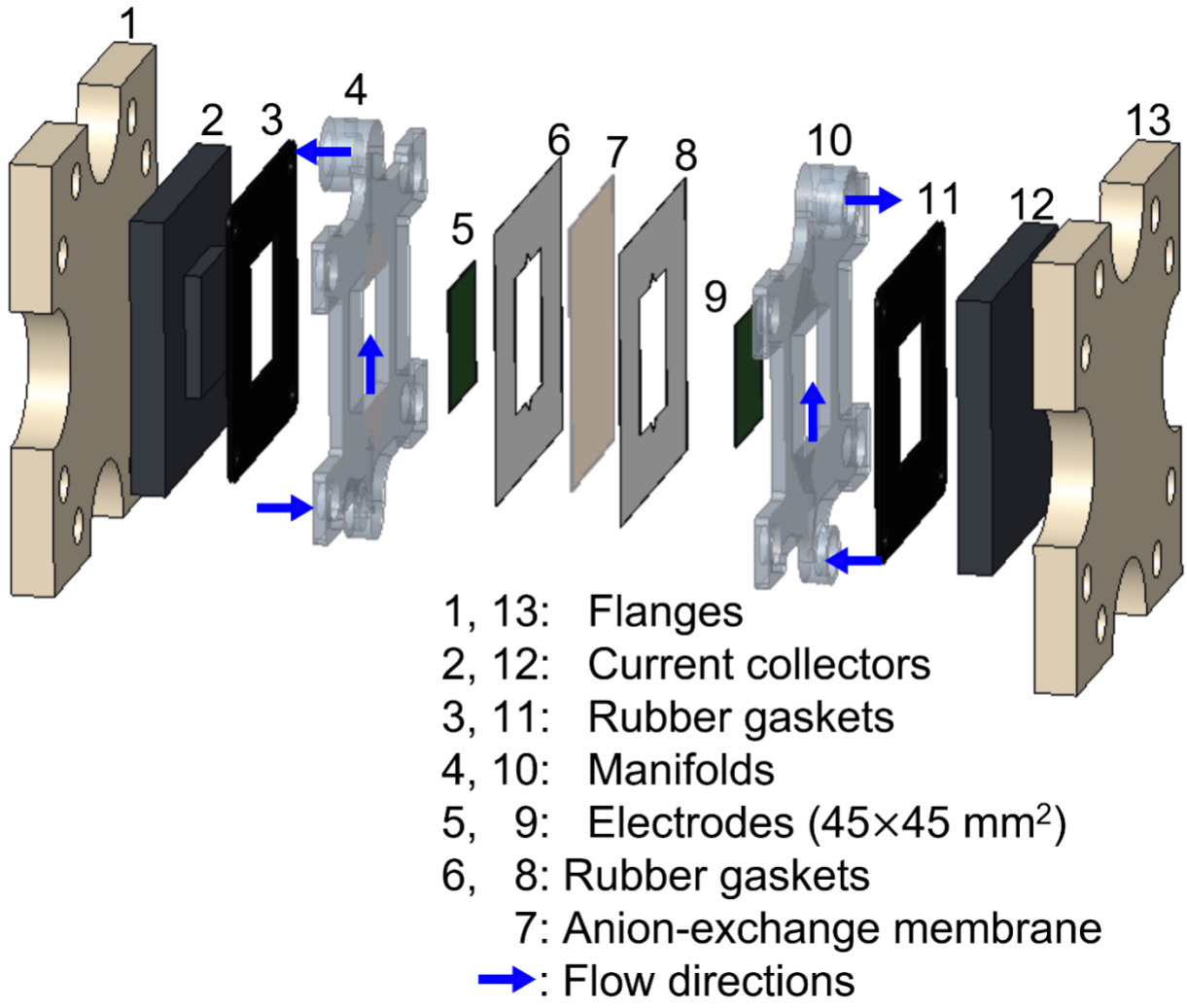

Figure S13: Components of the FDI flow cell.

Details of Desalination Performance

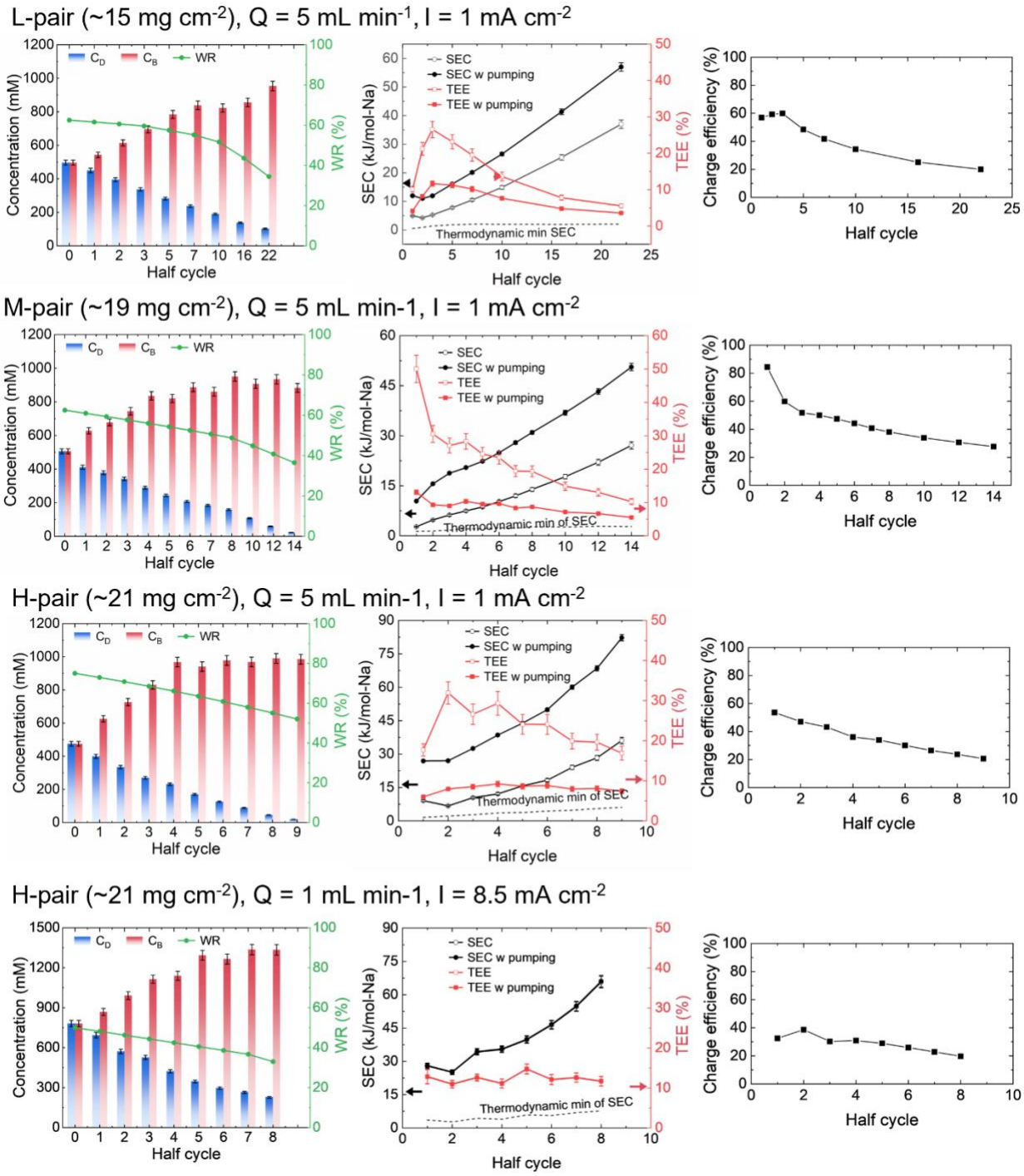

Figure S14: Detailed data for desalination experiments in Fig. 5a of the main text. Salt concentrations in diluate and brine reservoirs, specific energy consumption (SEC), thermodynamic energy efficiency (TEE), and charge efficiency versus half-cycle in desalination experiments with the electrodes and conditions shown.

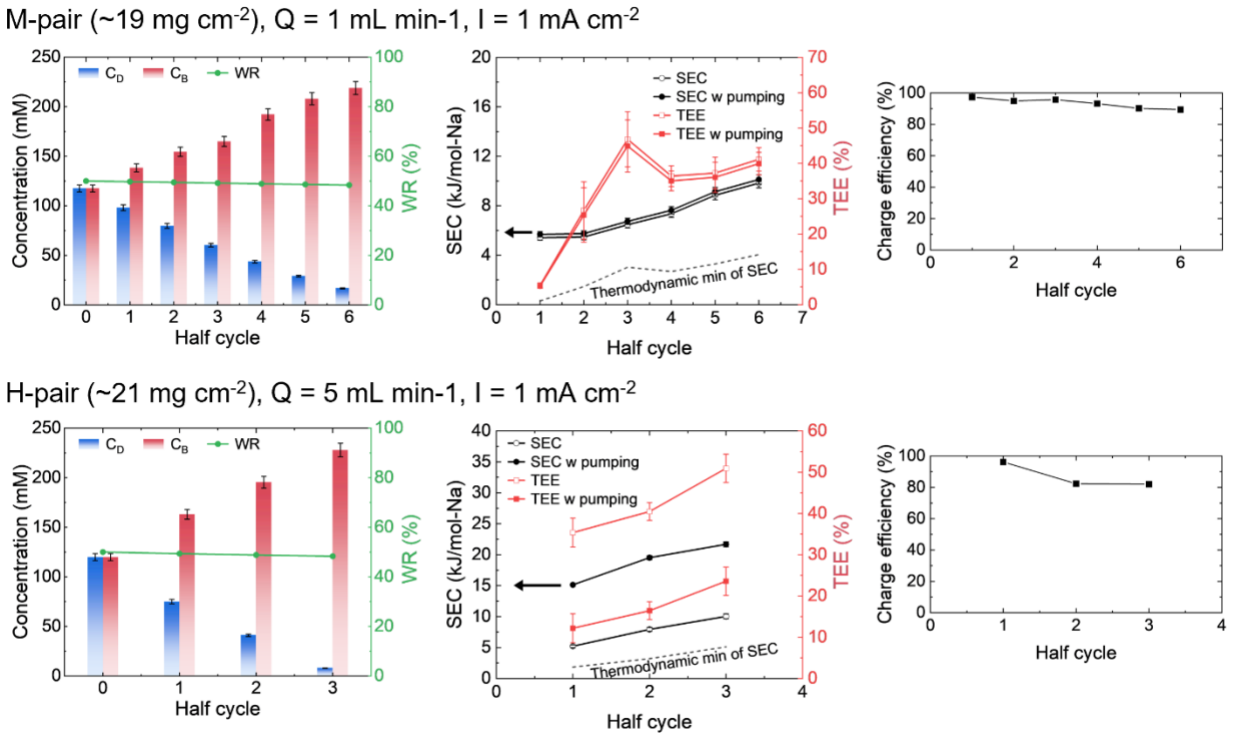

Figure S15: Detailed data for desalination experiments in Fig. 5b of the main text. Salt concentrations in diluate and brine reservoirs, SEC, TEE, and charge efficiency versus half-cycle in desalination experiments with the electrodes and conditions shown.

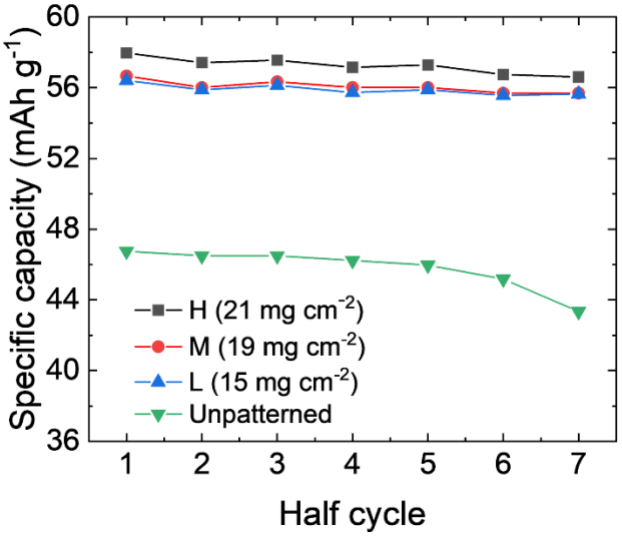

Figure S16. Specific capacity of patterned and unpatterned electrodes in an FDI cell with 500 mM NaCl feed concentration.

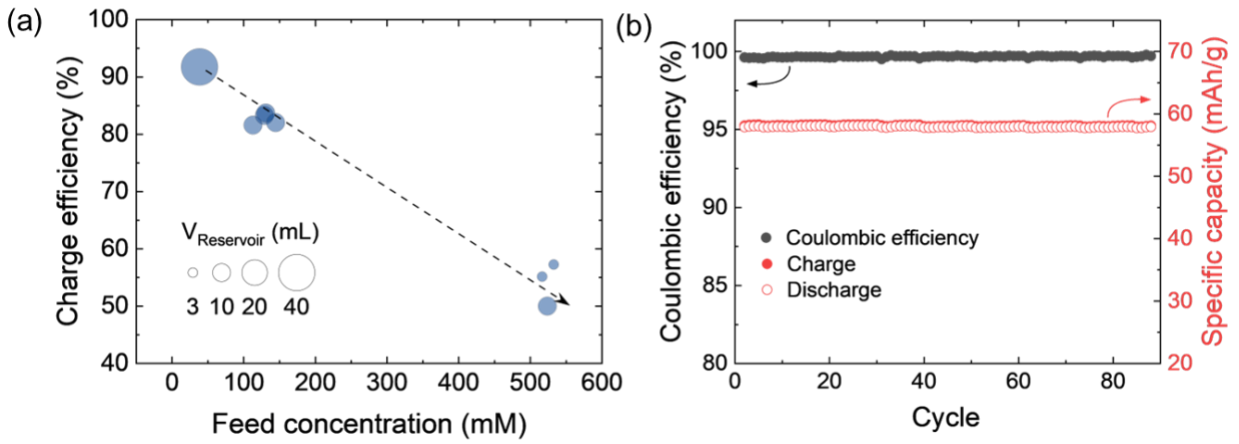

Figure S17. (a) Dependence of charge efficiency on feed concentration and reservoir volume. (b) Coulombic efficiency and specific capacity of electrodes. These experiments were performed using H-pair electrodes with 21 mg cm^{-2} areal loading.

Prior to each desalination experiment we assembled the FDI flow cell with a fresh piece of as-received Neosepta AMX anion exchange membrane (AEM) material, and each AEM was inspected visually after each desalination experiment *ex situ*. The AEMs used for each desalination experiment used to obtain the data in Fig. 4 showed no changes in color or texture. However, weak yellow discoloration of an AEM (Fig. S18) was observed after H-pair electrodes were cycled for 90 cycles in 500 mM NaCl to obtain the data in Fig. S7b. Previous work[3] implicated changes of Neosepta AMX from transparent to translucent yellow, orange, red, or black with dehydrochlorination of poly(vinyl chloride) to polyene due to alkali attack. We hypothesize that side reactions that produce OH^- during the instants that cell potential approaches its extreme (±0.4V) could be responsible for this degradative effect. Because the electrodes and the AEM are compressed within the flow cell, solution near the electrode/AEM interface may have reduced local fluid permeability, limiting access of fresh salt solution to their interface, leading to the local depletion of salt and thus promoting side reactions instead of cation intercalation. These observations therefore motivate detailed investigation of membrane longevity in FDI and the mechanisms that determine it. Because longer exposure time and higher NaOH concentration were shown previously to result in darker hues of Neosepta AMX undergoing alkali attack, the light yellow coloration observed in our present experiments indicates minimal AEM degradation that is likely a result of the galvanostatic cycling conditions (constant current) that we used in this work, rather than potentiostatic conditions (constant potential) that would hold the cell at extreme potentials for much longer time periods.

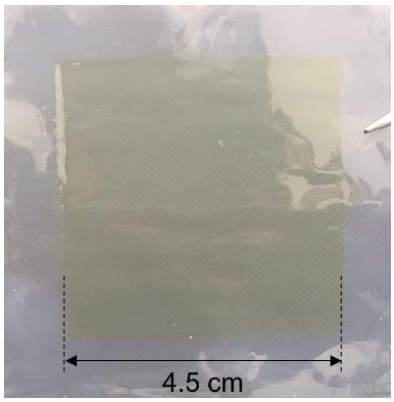

Figure S18. Photo of Neosepta AMX AEM after 90 cycles in a flow cell where the AEM was sandwiched between H-pair electrodes, as described in the caption of Fig. S7b.

Table S2. Data for Fig. 1a in the main text.

Author, year	Flow configuration	Electrode capacity (mAh)	Salt removal (mM)	Feed concentration (mM)	Ref.*
Kim et al., 2017	Flow by	0.24745	7.5	25	31
Ahn et al., 2021	Flow by	5.04	100	500	32
Son et al., 2020	flow-through vs flow-by	1.68	15	50	30
Pothanamkandathil et al., 2020	flow by	0.83333	5	20	29
Porada, 2017	flow by	47	0.5	20	33
Lee et al., 2017	batch	5.058	190.8	477	17
Reale 2019	flow through	0.6	27	100	28
Reale 2021	flow through	1.84	104	200	26
Reale 2021	flow through	1.84	90	100	26
This work		21.5	455.5	474.6	
This work		21.5	112	119.8	
This work		21.5	553	780	

* The reference number here refers to that in the main text.

Table S3: Data for Fig. 1b in the main text.

Flow Field Type	Notes	Cell Area (cm^2)	Channel Width (mm)	Flow Path (mm)	Ref*
SFF	-	25	1	1	50
PFF & IDFF	-	23	1.1	0.89	58
SFF & IDFF	-	N/A	1	1	60
SFF & IDFF	-	100-625	1-4	1-8	62
MSFF	Modified Serpentine	N/A	2	2	46
MSFF	Modified Serpentine	16-100	4	4	45
MSFF	Modified Serpentine	2200	5	2	66
IDFF	-	25	1	0.8	51
IDFF & MIDFF	Modified Interdigitated	900-1500	1	2-5	53
SFF	-	1500	3-5	2-3	65
SFF & IDFF	-	0.23	0.8	0.8	57
IDFF	-	10.24	1	1	56
IDFF	-	N/A	3	1-2.3	49
IDFF	-	4	1	1	59
IDFF	-	N/A	1	1	47
SFF	-	400-900	3-5	2-3	64
PFF & IDFF	-	10	1	1	52
IDFF & MIDFF	Modified Interdigitated	9-900	1	1	68
IDFF & MIDFF	Modified Interdigitated	39.84	1-3	1	44
SFF & IDFF	-	N/A	1	1	63
IDFF	-	625	2	3	61
IDFF	-	N/A	1	1	48
SFF	-	N/A	1	1	55
MPFF	Modified Parallel	N/A	0.2-0.8	0.25	70
SFF & IDFF	-	4	1	1	54
PFF	-	32	2	1	69
IDFF	-	20.25	0.07	0.5	This work

* The reference number here refers to that in the main text.

Table S4: Data for Fig. 1c in the main text.

	CDI (min)	CDI (max)	FDI flow-by (min)	FDI flow-by (max)	FDI flow-through (min)	FDI flow-through (max)	This work (min)	This work (max)
TEE (%)	0.1	3	5	40	5	40	3	40
E_{pump} (W h m^{-3})	0	0	0	0	0	50	0.005	1.2
SAC (mg g^{-1})	10	20	40	100	40	100	132.8	161.4
SAR (mg $g^{-1}min^{-1}$)	0.1	1	0.01	0.02	0.01	0.02	0.22	1.16
SR (mM)	0	5	0.5	100	15	104	394	554

Table S5: Raw data for Figs. 5a and 5b in the main text.

Electrodes	Feed concentration (mM)	Current density (mA cm^{-2})	Reservoir volume (mL)	Flow rate (mL min^{-1})	Dilutate concentration (mM)	Water transport (L $m^{-2}h^{-1}$)
L	496.4	1	5	5	102.4	0.095
M	496.4	1	5	5	23.7	0.107
H	496.4	1	5	5	19.1	0.148
H	780.9	8.5	5	1	227.5	0.159
M	118.0	1	30	5	16.7	-
H	119.8	1	30	5	7.8	-

References

1. Smith, K. C. Theoretical evaluation of electrochemical cell architectures using cation intercalation electrodes for desalination. *Electrochim. Acta* **230,** 333–341 (2017).
2. Liu, S. & Smith, K. C. Quantifying the trade-offs between energy consumption and salt removal rate in membrane-free cation intercalation desalination. *Electrochim. Acta* **271,** 652–665 (2018).
3. Doi, S., Yasukawa, M., Kakihana, Y. & Higa, M. Alkali attack on anion exchange membranes with PVC backing and binder: Effect on performance and correlation between them. *J. Memb. Sci.* **573,** 85–96 (2019).
4. Boussinesq, M. J. Mémoire sur l'influence des frottements dans les mouvements réguliers des fluides. *J. Math. Pure Appl.* **13,** 377–424 (1868).
5. NAPOV, A. & NOTAY, Y. AN ALGEBRAIC MULTIGRID METHOD WITH GUARANTEED CONVERGENCE RATE. *SIAM J. SCI. Comput.* **34,** A1079–A1109 (2012).
6. Yvan Notay. An aggregation-based algebraic multigrid method. *Electron. Trans. Numer. Anal.* **37,** 123–146 (2010).
7. NOTAY, Y. AGGREGATION-BASED ALGEBRAIC MULTIGRID FOR CONVECTION-DIFFUSION EQUATIONS. *SIAM J. SCI. Comput* **34,** A2288–A2316 (2012).